Chemical Physics Letters xxx (2013) xxx–xxx

Contents lists available at SciVerse ScienceDirect

Chemical Physics Letters

journal homepage: www.elsevier.com/locate/cplett

Chemical analysis using *J*-coupling multiplets in zero-field NMR

Thomas Theis [a,b,*,1], John W. Blanchard [a,b], Mark C. Butler [a,b,2], Micah P. Ledbetter [c], Dmitry Budker [c,d], Alexander Pines [a,b,*]

[a] Department of Chemistry, Duke University, 124 Science Drive, French Family Science Center, Room 2303, Durham, NC 27708, USA
[b] Department of Chemistry, University of California, Berkeley, 208C Stanley Hall, Berkeley, CA 94720-3220, USA
[c] Department of Physics, University of California at Berkeley, Berkeley, CA 94720-7300, USA
[d] Nuclear Science Division, Lawrence Berkeley National Laboratory, Berkeley, CA 94720, USA

ARTICLE INFO

Article history:
Received 26 April 2013
In final form 20 June 2013
Available online xxxx

ABSTRACT

Zero-field nuclear magnetic resonance (NMR) spectroscopy is emerging as a new, potentially portable, and cost-effective NMR modality with the ability to provide information-rich, high-resolution spectra. We present simple rules for analysis of zero-field NMR spectra based on first-order perturbation theory and the addition of angular momenta. These rules allow for the prediction of observed spectral lines without numerical simulation. Results are presented for a few small organic molecules with characteristic spin topologies, demonstrating unambiguous assignment of peaks, highlighting the potential of zero-field NMR as a tool for chemical identification.

1. Introduction

Low-field NMR techniques have been developed in the last decade with the promise of low-cost chemical analysis. The obtained low-field spectra have high information content similar to that of high-field NMR spectra. Much effort has been devoted to the interpretation of these NMR spectra acquired in magnetic fields ranging from zero field (below 1 μG) to elevated magnetic fields (~1 T) that are not large enough to be considered within the standard high-field regime of superconducting magnets [1–6]. In the low-field regime where chemical shift differences and *J*-coupling constants are of comparable magnitude the effect of the magnetic field does not fully truncate the transverse components of the *J*-coupling and the emerging spectral patterns quickly become complex [5]. In moving to zero-field, the effects of chemical shifts and differing gyromagnetic ratios (i.e. differences in Larmor frequency) are removed such that only the scalar *J*-couplings remain. The spectra can then have reduced complexity allowing for more straightforward interpretation [7]. Given the growing interest in zero-field NMR for low-cost chemical analysis [3,7–10] there is need for a tool to readily interpret and assign zero-field NMR spectra.

In recent publications we have demonstrated that many challenges associated with low- and zero-field NMR have been overcome [2,11–17]. For instance, we have shown that the low levels of thermal polarization can be greatly increased via parahydrogen-induced polarization (PHIP), a hyperpolarization technique, enabling NMR of low-concentration analytes [8,18]. Alternatively, and implemented here, prepolarization in a strong permanent magnet (~1 T or above) and subsequent pneumatic shuttling of the sample into the detection region is feasible. Furthermore, the addition of small magnetic fields can be used to easily recover the information lost by going to zero field [3].

Here we present a straightforward method of interpreting zero-field spectra associated with spin systems commonly found in organic molecules. The approach is based on treating the interaction between strongly coupled spins by a large *J*-coupling as the dominant contribution to the Hamiltonian. We refer to this interaction as the zero-order interaction, noting that at zero field all chemical-shift differences vanish which represents the strongest interaction in classical high-field NMR experiments. Weaker *J*-coupling interactions involving distant spins are treated as a perturbation. This perturbation produces splitting of the zero-order energy levels. This is analogous to the case of high-field NMR where the chemical-shift term is dominant and the scalar couplings are treated as perturbation.

2. Methods

Zero-field NMR experiments were conducted as previously described [3], but a brief description is provided here. Typically 100 μL of an isotopically-enriched neat liquid were placed in a 5 mm NMR tube. This sample was prepolarized in a 1.8 T permanent magnet (10 cm × 5 cm × 5 cm) and then shuttled into the

* Corresponding authors at: Department of Chemistry, Duke University, 124 Science Drive, French Family Science Center, Room 2303, Durham, NC 27708, USA.
E-mail addresses: tho.theis@gmail.com, thomas.theis@duke.edu (T. Theis), pines@berkeley.edu (A. Pines).
[1] Department of Chemistry, Duke University, Durham, NC 27708-0354, USA.
[2] William R. Wiley Environmental Molecular Sciences Laboratory, Pacific Northwest National Laboratory, Richland, WA 99352, USA.

0009-2614/$ - see front matter © 2013 Elsevier B.V. All rights reserved.
http://dx.doi.org/10.1016/j.cplett.2013.06.042

zero-field detection region, within a set of μ-metal magnetic shields (R = 10 cm, L = 35 cm). Inside of the magnetic shields, the magnetic field is reduced to the μG level with a set of compensation coils. After arriving in zero field a DC magnetic-field pulse is applied to the sample to excite NMR coherences. The resulting sample magnetization is detected with an atomic magnetometer, details of which are presented elsewhere [3,7,8,18–20]. The central component of the magnetometer is a $4 \times 2 \times 3$ mm microfabricated Rb-vapor cell, operated with IR lasers at 795 nm. The prepolarization region, the magnetic shields, and the miniaturized detector together form a compact unit, making this instrumentation promising for low-cost, portable NMR. All J-coupling constants used in the simulations are obtained by comparing exact numerical simulations with the experimental spectra and choosing the best fit by visual inspection. An additional technical detail is that absolute offsets of the signal, i.e. all zero-frequency components, are eliminated experimentally whereas the simulations show that some magnetization not subject to evolution may be induced.

3. Spin systems in zero-field NMR and their notation

Spin systems that give rise to zero-field NMR signals with nonzero frequencies include spins with distinct gyromagnetic ratios interacting via J-couplings. The simplest type of observed systems are XA_n groups where X is a spin with gyromagnetic ratio γ_X, and A_n represents a set of equivalent spins with gyromagnetic ratio $\gamma_A = \gamma_X$ which are coupled to X with a coupling constant J_{XA}. In this letter, X is either ^{13}C or ^{15}N, and A_n are protons. Anticipating the presence of a perturbation, we refer to the spectrum of an isolated XA_n system as a zero-order spectrum. These spectra are simple and can be readily understood, as discussed in the next section. In larger organic molecules, XA_n systems are perturbed by additional spins B_m forming $(XA_n)B_m$ spin systems, where the B_m spins also have the same gyromagnetic ratio as the A_n spins ($\gamma_B = \gamma_A$), i.e. B_m typically are additional protons. The relative strength of the coupling to the X spin distinguishes the spins A_n from the spins B_m. In this notation spins within the parentheses (X and A_n) are strongly coupled, and the spins outside the parentheses B_m are weakly coupled to the (XA_n) system. In organic molecules where X typically is a ^{13}C or a ^{15}N nucleus and A_n and B_m are protons (^{1}H), the one-bond coupling constants between X and A_n range from ~70 Hz to ~250 Hz. In such molecules the coupling constants between X and B_m or A_n and B_m are an order of magnitude weaker and typically <20 Hz. Note that our nomenclature differs from the standard Pople nomenclature [21,22] used at high magnetic fields, which is based on the magnitude of chemical-shift differences relative to J-couplings. The Pople notation is not applicable at zero magnetic field, because chemical shifts cannot be defined when the Larmor precession frequency is zero. Table 1 summarizes the nomenclature, along with the notation chosen for the angular momentum of the individual groups in the spin system. These angular momentum operators form the basis for the analysis of the spectra. The discussion here focuses on small organic molecules with simple spin topologies, but more complex topologies, for example, those containing aromatic structures, can also be analyzed in a similar fashion [23].

Table 1
Notation for spin systems and the associated angular momenta in zero-field NMR. Vector operators are bold and quantum numbers are italicized. For explanations of the quantum numbers see Section 4.

	Spin	Angular momentum	Sum of angular momenta
Heteronucleus	X	$\mathbf{S}$ $S = ½$	N/A
n spin(s) strongly coupled to X (typically ^{1}H)	A_n	$\mathbf{I}_A$ $(=\Sigma_n \mathbf{I}_n)$ I_A	$\mathbf{S} + \mathbf{I}_A = \mathbf{F}_A$ $F_A = \lvert S - I_A \rvert ... \lvert S + I_A \rvert$
m spin(s) weakly coupled to X and A (typically ^{1}H)	B_m	$\mathbf{I}_B(=\Sigma_m \mathbf{I}_m)$ I_B	$\mathbf{F}_A + \mathbf{I}_B = \mathbf{F}$ $F = \lvert F_A - I_B \rvert ... \lvert F_A + I_B \rvert$

4. Unperturbed XA_n systems in zero-field NMR

In this section we review zero-field spectra resulting from XA_n systems on the basis of simple rules governing addition of angular momenta. We show in Figure 1 the spectra of an XA group, an XA_2 group and an XA_3 group in formic acid-[^{13}C], formaldehyde-[^{13}C], and methanol-[^{13}C], respectively. The XA group produces one line at frequency J_{XA}, the XA_2 group produces one line at $3/2 \times J_{XA}$, and the XA_3 group produces lines at J_{XA} and $2 \times J_{XA}$ [5,7].

Note that in most common organic molecules n does not exceed 3, and thus the number of lines in XA_n systems is small. However, the treatment easily extends to systems with $n > 3$. For odd n, an XA_n system produces $(n + 1)/2$ lines at frequencies ranging from J_{XA} to $(n + 1)/2 \times J_{XA}$ in steps of J_{XA}. For even n, the number of lines is $n/2$, with frequencies ranging from $3/2 \times J_{XA}$ to $(n + 1)/2 \times J_{XA}$ in steps of J_{XA}.

The appearance of these zero-order spectra can be explained from the rules governing the addition of angular momenta, which are briefly reviewed. As shown in Table 1 we denote the angular momentum of spin X as S and the angular momentum of the spins A_n as $\mathbf{I}_A = \Sigma_n \mathbf{I}_n$. The quantum number S equals 1/2 in all cases discussed here. The quantum number I_A ranges, in integer steps, from

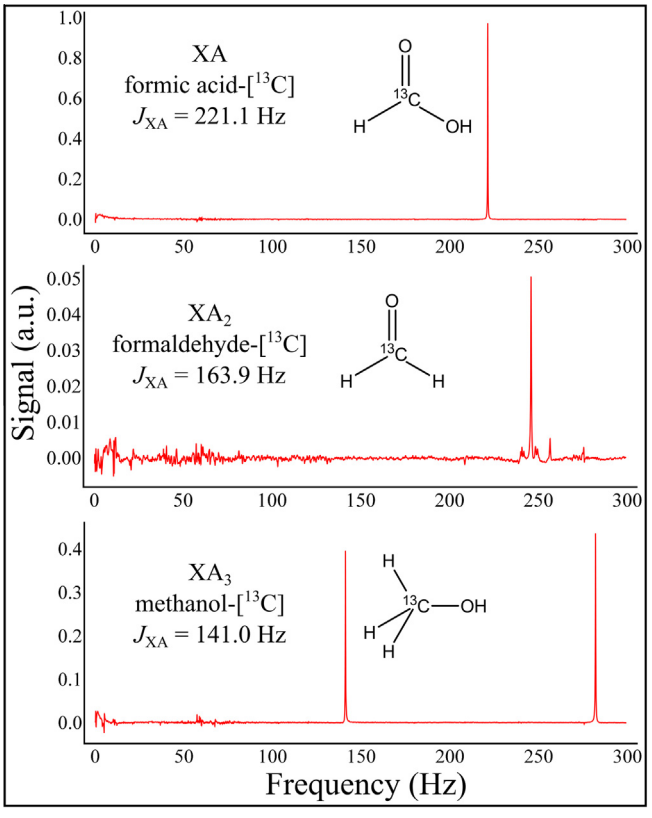

Figure 1. Zero-field NMR spectra of formic acid-[^{13}C], formaldehyde-[^{13}C] and methanol-[^{13}C] as examples of XA_n systems with $n = 1$, 2 and 3 respectively. Linewidths frequently are less than 20 mHz because of the easily-achieved zero-field homogeneity. The presented spectra are line-broadened to 0.2 Hz by multiplication of the FID with a decaying exponential for increased signal-to-noise. The formaldehyde-[^{13}C] spectrum contains sidebands around the main peak likely produced from formaldehyde hydrate or other impurities. (While the intensity units are arbitrary they are consistent for the three spectra.).

0 to $n/2$ for even n, and from 1/2 to $n/2$ for odd n. We introduce $\mathbf{F}_A$ as the sum of $\mathbf{I}_A$ and $\mathbf{S}$, such that the associated quantum number F_A ranges from $|I_A - S|$ to $I_A + S$ in integer steps. The energy levels in XA_n systems are fully determined by the three quantum numbers S, I_A, and F_A. These energy levels are shown, in Figure 2, for the XA, XA_2 and XA_3 systems. Each F_A-energy-level manifold has a degeneracy of $(2F_A + 1)$ because of the possible values of the z-component, m_{FA} of the angular momentum $\mathbf{F}_A$. The quantum number m_{FA} ranges from $+F_A$ to $-F_A$. This degeneracy is only lifted in the presence of a magnetic field [3]. The energy of each F_A-manifold is given by [7,24] Suppl.Inf.

$$E^0 = \frac{J_{XA}}{2}[F_A(F_A+1) - I_A(I_A+1) - S(S+1)], \quad (1)$$

resulting in the simple structure of the energy levels. When evaluating Eq. (1) we obtain $(n + 1)$ energy eigenvalues which range from $-J_{XA} \times (n/4 + 1/2)$ to $+J_{XA} \times n/4$. The eigenvalues are spaced by $J_{XA}/2$. For odd n, however, the value of $-1/4 \times J_{XA}$ does not appear as an eigenvalue, and for even n the value of $-1/2 \times J_{XA}$ does not appear as an eigenvalue.

Next, in order to arrive at the observed transitions, we employ the selection rules found for observable magnetization along the z axis. Then, the selection rules can be derived as [7,24] Suppl.Inf.

$$\Delta I_A = 0; \quad \Delta S = 0; \quad \Delta F_A = \pm 1; \text{ and } \Delta m_{F_A} = 0. \quad (2)$$

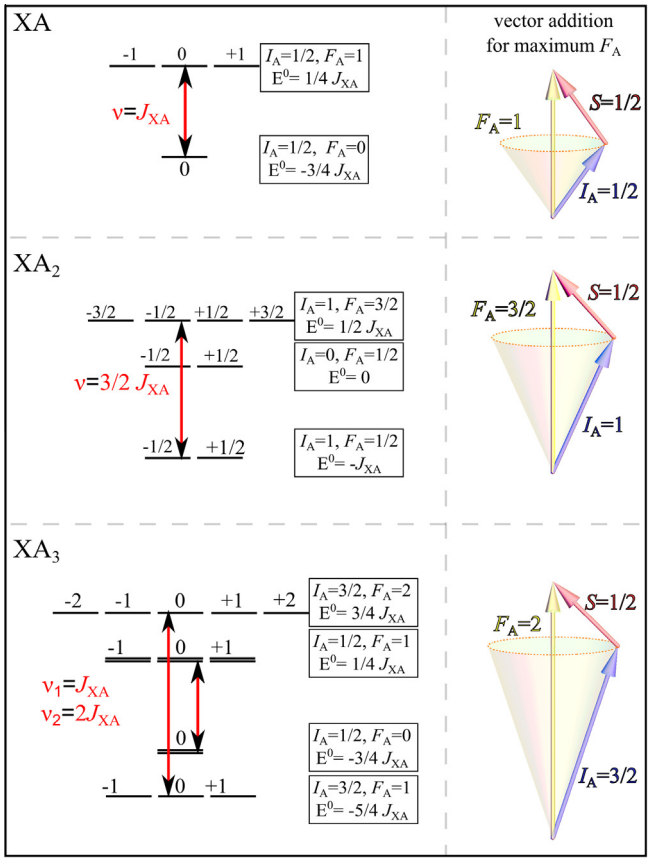

Figure 2. Energy level diagrams for XA_n systems with $n = 1, 2, 3$. Each manifold is labeled by its characteristic quantum numbers. ($S = 1/2$ for all manifolds.) Energy levels in each angular momentum manifold are labeled with their magnetic quantum number m_{FA}. Red arrows show allowed transitions. For sake of clarity transitions are only shown for one value of m_F. Next to the energy-level diagram a geometrical depiction of addition of angular momentum is provided for the case of maximum F_A. The length of all arrows is given as $\sqrt{K}(K+1)$ where K refers to the respective quantum number (S, I_A or F_A). Note, that in this and all subsequent figures closely spaced energy levels are degenerate. (For interpretation of the references to colour in this figure legend, the reader is referred to the web version of this article.)

using the selection rules from Eq. (2) we find that the allowed transitions occur exactly at the frequencies described earlier. The transition frequencies can be expressed in the form $\nu = J_{XA}(F_A + 1/2)$ for $F_A \geqslant 1/2$, where F_A ranges from 0 (for odd n) or 1/2 (for even n) to $(n + 1)/2$. Note that the selection rule for Δm_{FA} is inconsequential because all m_{FA} states within a manifold of F_A are degenerate at zero field. (see Suppl.Inf. for more details.)

For additional insight, the origin of the energy-level manifolds can be illustrated with vector pictures shown on the right side of Figure 2. $\mathbf{F}_A$ is shown as the sum of $\mathbf{I}_A$ and $\mathbf{S}$. The total angular momentum $\mathbf{F}_A$ is a conserved quantity at zero magnetic field and $\mathbf{I}_A$ and $\mathbf{S}$ can be visualized as precessing about F_A. For each energy-level manifold the angular momenta can be represented by vectors of length $\sqrt{K}(K+1)$, where K refers to the respective quantum number (S, I_A or F_A). The addition of angular momenta is represented as vector addition by arranging the vectors in a triangle such that $\mathbf{I}_A + \mathbf{S} = \mathbf{F}_A$. [26] These representations are shown only for those manifolds with maximum F_A. The vectors obey the triangle selection rule: $|I_A - S| \leqslant F \leqslant I_A + S$ [26]. Only those values of F are allowed for which it is possible to form a triangle with length I_A, S and F.

To avoid confusion we point out that these vector pictures are constructed for individual degenerate manifolds, and the precession frequency of the summed angular momenta about their respective sum is not directly related to the observed precession of the magnetization in the sample. The cones represent quantum–mechanical uncertainty in the components of $\mathbf{I}_A$ and $\mathbf{S}$ transverse to $\mathbf{F}$ [27].

5. $(XA_n)B_m$ Systems in zero-field NMR

The effects on the spectra of additional spins coupling into XA_n systems are additional line splittings of the zero-order spectra. We will analyze typical $(XA_n)B_m$ systems and compare the predictions with experimental results. To zero order, the $(XA_n)B_m$ systems are determined solely by the strong one-bond coupling J_{XA}. The first-order interactions result from additional J-couplings through at least two bonds. This situation is amenable to analysis with a first-order approach because the separation between strong and weak couplings is roughly an order of magnitude.

The simplest case of a perturbed XA_n system is the $(XA)B$ system. The analysis of this system will serve as an introduction to the more general cases. Figure 3a shows a simulated spectrum of the $(XA)B$ system using typical coupling constants found in organic molecules (J_{XA} = 150 Hz, J_{XB} = −4 Hz J_{AB} = 8 Hz). The zero-order peak nominally at J_{XA} is now split into two lines separated by $3/4 \times (J_{XB} + J_{AB})$. Additionally a low-frequency peak at $3/4 \times (J_{XB} + J_{AB})$ is observed.

Figure 3(c) shows the corresponding energy-level diagram for the $(XA)B$ system. We introduce the quantum operators $\mathbf{I}_B$ and $\mathbf{F}$ (see Table 1), where $\mathbf{I}_B$ ($=\Sigma_m \mathbf{I}_m$) is the angular momentum operator of the B_m group and $\mathbf{F} = \mathbf{F}_A + \mathbf{I}_B$ is the total angular momentum operator with quantum numbers F ranging from $|F_A - I_B|$ to $F_A + I_B$. Addition of spin B splits the zero-order energy level of the XA system with $F_A = 1$ into two manifolds with total angular momentum $F = 3/2$ and $F = 1/2$. The zero-order energy level with $F_A = 0$ is replaced by an energy level with total angular momentum $F = 1/2$. Note that the resulting manifolds of F are associated with $2F + 1$ values of m_F, the z-component of the total angular momentum F. The quantum number m_F ranges from $+F$ to $-F$. The degeneracy between states with different m_F is only lifted in the presence of a magnetic field [3].

We are now considering the first-order energy shifts, which can be understood on the basis of a simple projection. This is illustrated in Figure 3b, which depicts the total angular momentum $\mathbf{F}$ as sum of $\mathbf{F}_A$ and $\mathbf{I}_B$. $\mathbf{F}_A$ is depicted as the sum of $\mathbf{S}^{||}$ and $\mathbf{I}^{||}{}_A$ which are the projections of $\mathbf{S}$ and $\mathbf{I}_A$ onto $\mathbf{F}_A$. The angular momentum $\mathbf{I}_B$ interacts

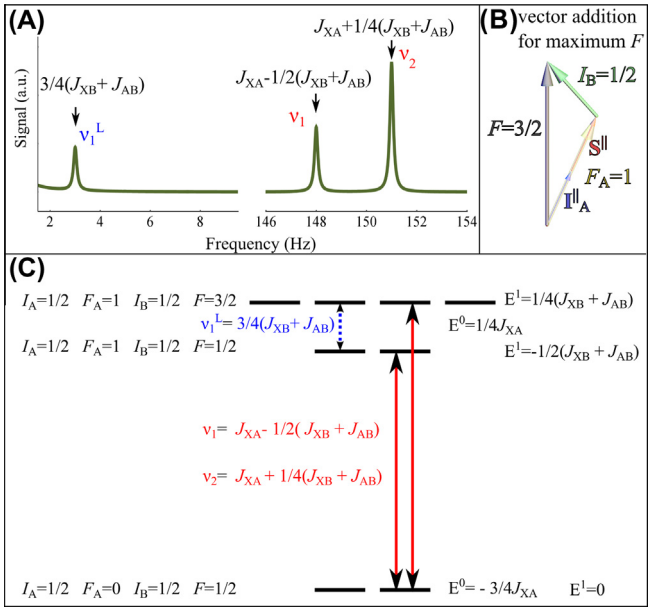

Figure 3. (a) Simulated zero-field spectrum of an $(XA)B$ system based on first-order perturbation theory. The high-frequency line expected of an XA system is split into two lines and an additional low-frequency line is observed. The relative intensities are, from low to high frequency, 2:3:6. (b) Geometrical depiction of the addition of angular momentum $\mathbf{I}_B$ to the angular momentum $\mathbf{F}_A$ of the XA system, which gives the total angular momentum $\mathbf{F}$. In this illustration $\mathbf{S}^{\|}$ and $\mathbf{I}^{\|}_A$ represent the projections of $\mathbf{S}$ and $\mathbf{I}_A$ onto $\mathbf{F}_A$. Cones illustrating the precession are omitted for clarity. (c) Energy level diagram for the $(XA)B$ system. The observed transitions at high frequencies are shown with red arrows, and the additional low-frequency transition is indicated by the blue dashed arrow. (For interpretation of the references to colour in this figure legend, the reader is referred to the web version of this article.)

with the projections $\mathbf{S}^{\|}$ and $\mathbf{I}^{\|}_A$ rather than with $\mathbf{S}$ or $\mathbf{I}_A$ directly. This is because for a coupling constant $J_{XA} >> (J_{XB}, J_{AB})$, the precession frequencies of $\mathbf{I}_A$ and $\mathbf{S}$ about $\mathbf{F}_A$ is large relative to the precession frequencies of $\mathbf{I}_B$ and $\mathbf{F}_A$ about $\mathbf{F}$. Therefore, to first order, $\mathbf{I}_B$ only interacts with the average of $\mathbf{S}$ and $\mathbf{I}_A$ given by $\mathbf{S}^{\|}$ and $\mathbf{I}^{\|}_A$. The first-order energies are evaluated using this approximate description of the interaction [24] Suppl.Inf.

Whenever $F_A = 0$, the first-order energy shift is always zero because the projection of $\mathbf{I}_A$ or $\mathbf{S}$ onto an angular-momentum with $F_A = 0$ is zero. Only energy levels with $F_A > 0$ will be affected by the additional couplings from the B_m group. As shown in Figure 3c the first-order energy shifts E^1 to the $F_A = 1$ manifold are given as $E^1 = 1/4 \times (J_{XB} + J_{AB})$ for $F = 3/2$ and $E^1 = -1/2 \times (J_{XB} + J_{AB})$ for $F = 1/2$. In deriving these expressions the projection of $\mathbf{I}_A$ and $\mathbf{S}$ onto $\mathbf{F}_A$ is used, resulting in a scaling of the J-couplings [24]. In the present case J_{XB} and J_{AB} are scaled by the same amount because $S^{\|}$ and $I^{\|}_A$ have the same length.

Finally, Figure 3c also shows the observed transitions. Here and in all subsequent images, red arrows indicate high-frequency lines with $\Delta F_A = \pm 1$ and blue arrows indicate low-frequency lines with $\Delta F_A = 0$. Note that transitions are always shown for one value of m_F only to avoid overcrowding of the images.

In order to predict the observed transitions the appropriate selection rules need to be invoked, which, for magnetization along z, are given as [24] Suppl.Inf.

$$\Delta I_A = 0;\ \ \Delta I_B = 0;\ \ \Delta F_A = 0, \pm 1;\ \Delta F = 0, \pm 1;\ \textit{and}\ \Delta m_F = 0. \qquad (3)$$

In the case of $(XA)B$, each pair of manifolds participates in a transition. The zero-order peak for which $\Delta F_A = 1$ is split by $3/4 \times (J_{XB} + J_{AB})$. The relative intensity of these two peaks is 1:2. The peak at low frequency is due to $\Delta F_A = 0$ transitions between the two $F_A = 1$ manifolds.

Having summarized the main features of the spectrum obtained from the $(XA)B$ system, we now move to the general description of $(XA_n)B_m$ systems.

Using the projection of angular momenta a formula is derived for all first-order energy shifts in $(XA_n)B_m$ systems, giving access to the first-order positions of all angular-momentum manifolds and hence all frequencies. The first order shifts are given by [24] Suppl.Inf.

$$E^1 = \frac{J^{\|}_{XB} + J^{\|}_{AB}}{2}[F(F+1) - F_A(F_A+1) - I_B(I_B+1)], \qquad (4)$$

where

$$J^{\|}_{XB} = \frac{J_{XB}}{2}\left[1 + \frac{S(S+1) - I_A(I_A+1)}{F_A(F_A+1)}\right], \qquad (5)$$

$$J^{\|}_{AB} = \frac{J_{AB}}{2}\left[1 + \frac{I_A(I_A+1) - S(S+1)}{F_A(F_A+1)}\right]. \qquad (6)$$

Comparing Eqs. (4)–(6) reveals that the structure of the two equations is identical except that the J-coupling constant J_{XA} has been replaced by the sum of the scaled J-coupling constants $J^{\|}_{XB}$ and $J^{\|}_{AB}$ given in Eqs. (5) and (6). This scaling of the coupling constants can be understood geometrically: it is the result of projecting $\mathbf{I}_A$ and $\mathbf{S}$ onto $\mathbf{F}_A$. $\mathbf{I}_B$ now interacts with these 'smaller' spins $\mathbf{I}^{\|}_A$ and $\mathbf{S}^{\|}$ and the J-couplings are scaled. The intensity of the signal is proportional to $(\gamma_A - \gamma_X)^2$. The relative intensities are given by sums over Clebsch–Gordan coefficients and can be calculated as such for the general $(XA_n)B_m$ system [24] Suppl.Inf. These relative intensities result as ratios of small integer numbers and are provided in the figure captions.

The experimental spectra presented below and in the SI can be analyzed following the same algorithm: first, the different values for I_A are found, and $S = 1/2$ is added to each of these to obtain the values of F_A. This gives the zero-order structure of the energy-level diagram. Second, the different values for I_B are found and each of these are added to each F_A to obtain the values of F. Lastly, the energy of each manifold is obtained using Eq. (4) and the transitions are found using the selection rules given in Eq. (3). Here we present the spectra of methylformate-[^{13}C] and formamide-[^{15}N] in order to illustrate the method. In the SI three additional examples are discussed: ethanol-[1−^{13}C], ethanol-[2−^{13}C], and glycerol-[2−^{13}C].

Figure 4 shows the experimental spectrum of methylformate-[^{13}C], which constitutes an $(XA)B_3$ system. Plotted below the experimental spectrum are a first-order simulation and an exact numerical simulation. In this case, both the first-order and the exact numerical simulation agree well with the experimental spectrum. The zero-order spectrum for an unperturbed AX system would consist of a single peak at 226.5 Hz. This peak is split into four lines by the additional couplings J_{XB} and J_{AB}. The strong J_{XA} coupling is 70 times larger than the sum of J_{XB} and J_{AB}, and so it is not surprising that the spectrum is well-reproduced by the first-order approximation.

The angular-momentum manifolds can be obtained using the values $S = 1/2$, $I_A = 1/2$ and $I_B = (1/2 \text{ or } 3/2)$. To zero order this system has the angular momentum manifolds of an XA system with $F_A = 0$ and $F_A = 1$, which are then perturbed by $I_B = 1/2$ or $I_B = 3/2$. The case of $I_B = 1/2$ has already been fully described for the $(XA)B$ system and, accordingly, we find peaks at all the expected positions for the $(XA)B$ system. These are $\nu_1{}^L$ at low frequency and ν_2 and ν_3 at high frequency. In addition, we observe two more peaks at high frequency (ν_1 and ν_4) and one additional low-frequency peak ($\nu_2{}^L$). These additional lines (ν_1, ν_4, $\nu_2{}^L$) result from the $I_B = 3/2$ configuration which generates additional angular momentum manifolds. Employing the selection rules as introduced in Eq.

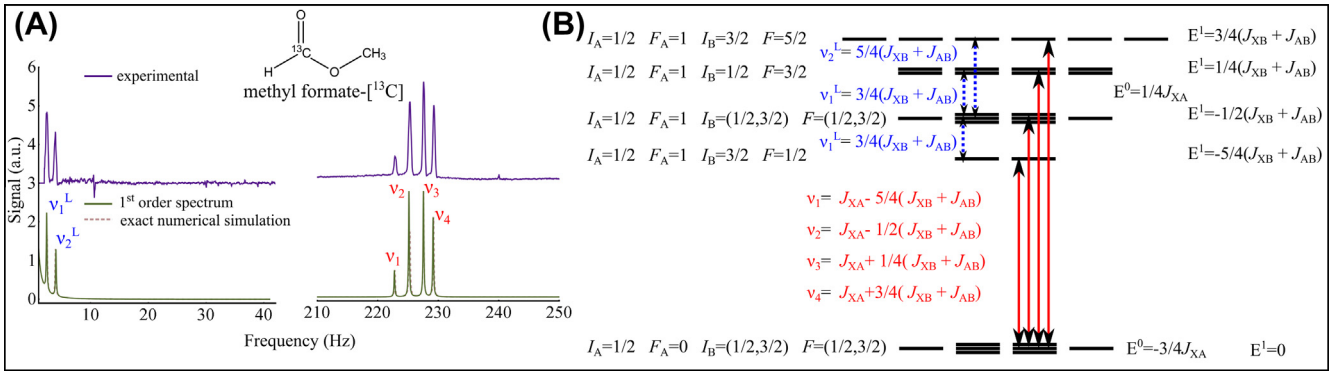

Figure 4. (a) Experimental spectrum of an $(XA)B_3$ system, methyl formate-[^{13}C], together with simulations to first order and exact numerical simulations. The J-coupling values used for the simulations are J_{XA} = 226.5 Hz, J_{XB} = 4.0 Hz and J_{AB} = −0.8 Hz. The relative intensities within each multiplet are (5:3)×3 for the low-frequency lines and (1:4:4:3)×5 for the four high-frequency lines centered on J_{XA}. The multiplicative factors scale the multiplets relative to each other. (b) Energy-level diagram for the $(XA)B_3$ system together with energies evaluated using Eqs. (1) and (4). The observed transitions at high frequencies are shown with red arrows, the low-frequency transitions are indicated by blue dashed arrows. (For interpretation of the references to colour in this figure legend, the reader is referred to the web version of this article.)

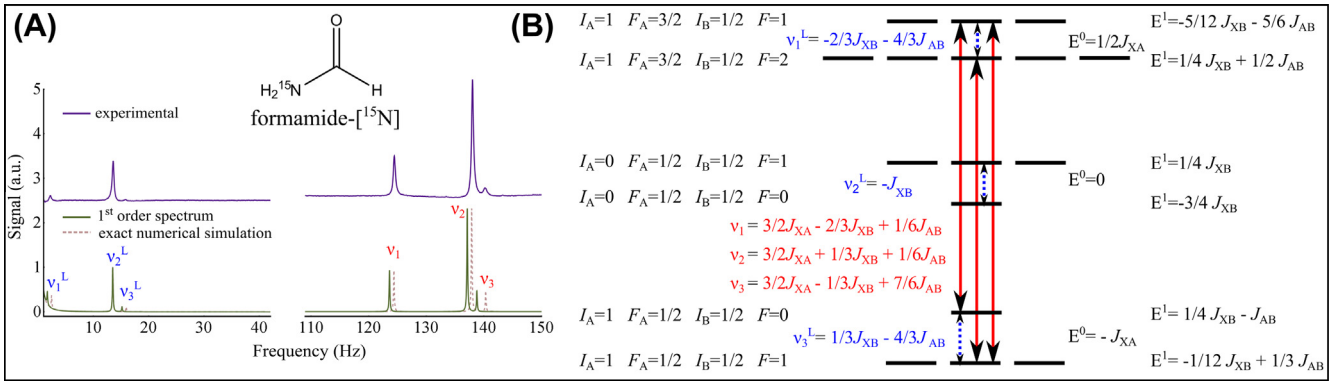

Figure 5. (a) Experimental spectrum of an $(XA_2)B$ system, formamide-[^{15}N], together with first-order and exact numerical simulations. The J-couplings used for simulation are J_{XA} = 89.3 Hz, J_{XB} = 13.5 Hz and J_{AB} = −8 Hz. The relative intensities (5:18:3)×1 for the three low-frequency lines and (2:5:1)×8 for the three high-frequency lines centered around $(3/2)J_{XA}$. The multiplicative factors scale the multiplets relative to each other. (b) Energy-level diagram for the $(XA_2)B$ system together with energies evaluated using Eqs. (1) and (4). The observed transitions at high frequencies are shown with red arrows, the low-frequency transitions are indicated by blue dashed arrows. (For interpretation of the references to colour in this figure legend, the reader is referred to the web version of this article.)

(3), the additional lines are found to be at frequencies $J_{XA}-5/4\times(J_{XA}+J_{XB})$ and $J_{XA}+3/4\times(J_{XA}+J_{XB})$. The additional low-frequency line occurs at $5/4(J_{XA}+J_{XB})$. In a higher-resolution experimental spectrum, we observe splitting due to higher-order effects of the line at ν_2 and $\nu_1{}^{L}$ because higher-order effects split the energy levels [24] that appear degenerate at $E^1 = 1/2\times(J_{XB}+J_{AB})$.

Figure 5a shows the experimental and simulated spectra for formamide-[^{15}N], which constitutes an $(XA_2)B$ system. The zero-order peak expected at $3/2\times J_{XA}$ is split into three lines; also three additional low-frequency lines are observed. All observed frequencies for the $(XA_2)B$ system are listed in Figure 5b, and the intensities are listed in the caption. As can be seen from Figure 5a the higher-order corrections are larger in this case than in methylformate, due to the smaller ratio between the strong one-bond coupling J_{XA} and the weaker long-range couplings J_{XB} and J_{AB}.

It is worth noting that for the central energy levels where $F_A = 1/2$, we only expect a contribution from J_{XB} and none from J_{AB} because $I_A = 0$ and therefore $\mathbf{I}_B$ only interacts with $\mathbf{S}^{||}$ and not with $\mathbf{I}^{||}{}_A$ in this manifold. In this central manifold, the first-order energy shifts are $E^1 = -3/4\times J_{XB}$ for the singlet and $1/4\times J_{XB}$ for the triplet in analogy to the zero-order energy levels for the XA system.

It is also worthwhile to note that for all other manifolds the contribution to the energy shifts from J_{XB} and J_{AB} is asymmetric because $\mathbf{I}_A$ and $\mathbf{S}$ have differing projections onto $\mathbf{F}_A$.

5. Conclusion

Zero-field NMR is emerging as a cost-effective, potentially miniaturizable spectroscopic method. We have demonstrated that perturbation theory can be used to analyze zero-field NMR spectra in a methodical way, allowing for analysis of spectra without numerical simulations. A visualization of how the network of J-couplings is responsible for the zero-field spectra has been presented, giving geometrical insight into zero-field NMR spectra. When the spin operators of two strongly coupled spins ($\mathbf{I}$ and $\mathbf{S}$) are projected onto their sum ($\mathbf{F}_A$), the J-couplings are scaled down due to the fact that additional spins ($\mathbf{I}_B$) that weakly couple into the J-coupling network interact with the projections onto $\mathbf{F}_A$, rather than with $\mathbf{I}$ and $\mathbf{S}$ directly. This procedure is equivalent to a formal calculation of the first-order energy shifts but appears more intuitive because of geometric arguments. With the knowledge of simple expressions for the peak positions Eq. (4), assignment of peaks to chemical groups becomes feasible. For mixtures of chemicals, only a small amount of overlap is expected, given the typical sub-Hertz resolution of zero-field NMR and the large variations in one-bond coupling constants, which spread the observed multiplets widely. As demonstrated in the examples, peaks occur at largely varying frequencies because the observed multiplets are very sensitive to the chemical structure and the spin topology of individual molecules. The successful interpretation of zero-field J-spectra

represents another step toward making zero-field NMR attractive for applications ranging from bench-top chemical analysis to sample analysis in environments previously inaccessible by NMR.

Acknowledgments

Research was supported by the U.S. Department of Energy, Office of Basic Energy Sciences, Division of Materials Sciences and Engineering under Contract No. DE-AC02-05CH11231. Additionally, J.W. Blanchard is supported by a National Science Foundation Graduate Research Fellowship under Grant No. DGE-1106400. The mentioned sponsors had no involvement in study design; in the collection, analysis and interpretation of data; in the writing of the report; and in the decision to submit the article for publication.

Appendix A. Supplementary data

Supplementary data associated with this article can be found, in the online version, at http://dx.doi.org/10.1016/j.cplett.2013.06.042.

References

[1] S. Appelt, F.W. Häsing, H. Kühn, U. Sieling, B. Blümich, Chem. Phys. Lett. 440 (2007) 308.
[2] S. Appelt, S. Glöggler, F.W. Häsing, U. Sieling, A.G. Nejad, B. Blümich, Chem. Phys. Lett. 485 (2010) 217.
[3] M.P. Ledbetter et al., Phys. Rev. Lett. 107 (2011) 107601.
[4] S. Appelt, F. Häsing, H. Kühn, B. Blümich, Phys. Rev. A 76 (2007) 1.
[5] S. Appelt, F.W. Häsing, U. Sieling, A. Gordji-Nejad, S. Glöggler, B. Blümich, Phys. Rev. A 81 (2010) 1.
[6] S. Appelt, H. Kühn, F.W. Häsing, B. Blümich, Nat. Phys. 2 (2006) 105.
[7] M.P. Ledbetter et al., J. Magn. Reson. 199 (2009) 25.
[8] T. Theis et al., Nat. Phys. 7 (2011) 571.
[9] M.P. Ledbetter et al., Proc. Natl. Acad. Sci. USA 105 (2008) 2286.
[10] N. Kelso et al., J. Magn. Reson. 200 (2009) 285.
[11] J.N. Robinson, A. Coy, R. Dykstra, C.D. Eccles, M.W. Hunter, P.T. Callaghan, J. Magn. Reson. 182 (2006) 343.
[12] M.E. Halse, P.T. Callaghan, J. Magn. Reson. 195 (2008) 162.
[13] S. Appelt, F. Häsing, H. Kühn, J. Perlo, B. Blümich, Phys. Rev. Lett. 94 (2005) 1.
[14] B. Blümich, F. Casanova, S. Appelt, Chem. Phys. Lett. 477 (2009) 231.
[15] S. Glöggler, M. Emondts, J. Colell, R. Müller, B. Blümich, S. Appelt, The Analyst 136 (2011) 1566.
[16] A.H. Trabesinger, R. McDermott, S. Lee, M. Mu, J. Clarke, A. Pines, J. Phys. Chem. A 108 (2004) 957.
[17] R. McDermott, A.H. Trabesinger, M. Muck, E.L. Hahn, A. Pines, J. Clarke, Science 295 (2002) 2247.
[18] T. Theis et al., J. Am. Chem. Soc. 134 (2012) 3987.
[19] D. Budker, M. Romalis, Nat. Phys. 3 (2007) 227.
[20] I.K. Kominis, T.W. Kornack, J.C. Allred, M.V. Romalis, Nature 422 (2003) 596.
[21] H.J. Bernstein, J.A. Pople, W.G. Schneider, Can. J. Chem. 35 (1957) 65.
[22] J.A. Pople, T. Schaefer, Mol. Phys. 3 (1960) 547.
[23] J.W. Blanchard, M.P. Ledbetter, T. Theis, M.C. Butler, D. Budker, A. Pines, J. Am. Chem. Soc. 135 (2013) 3607.
[24] M.C. Butler, M.P. Ledbetter, T. Theis, J.W. Blanchard, D. Budker, A. Pines, J. Chem. Phys. 138 (2013) 184202.
[26] C. Cohen-Tannoudji, B. Diu, D. Ostrowsky, Quantum Mechanics, Wiley, New York, 1977.
[27] M. Auzinsh, D. Budker, and S. M. Rochester, Optically Polarized Atoms: Understanding Light–Atom Interactions, illustrate (Oxford University Press, 2010).